Invited Paper

Near-Infrared Electroluminescence of Furnace or CO_2 Laser Annealed Si-rich SiO_2 with Structural Defects and Si Nanocrystals

Gong-Ru Lin and Chun-Jung Lin

Department of Photonics & Institute of Electro-Optical Engineering,
National Chiao Tung University
1001, Ta Hsueh Road, Hsinchu 300, Taiwan R.O.C.
Phone: 886-3-5712121 ext.56376; Fax: 886-3-5716631
E-mail: grlin@faculty.nctu.edu.tw

ABSTRACT

Electroluminescence of the CO_2 laser annealed PECVD-grown silicon-rich silicon oxide (SRSO) based metal-oxide-semiconductor diode with embedded Si nanocrystals is demonstrated. The structural and optical properties of a CO_2 laser rapid thermal annealed Si-rich $SiO_{1.25}$ film are investigated. The color of $SiO_{1.25}$ film changes from light yellow to dark-yellow as the CO_2 laser annealing intensity enlarges from 1.5 to 13.5 kW/cm^2. Such a color change is mainly attributed to both the increasing absorption coefficient and refractive index of the $SiO_{1.25}$ film under the precipitation of Si nanocrystals. The thickness of the $SiO_{1.25}$ film was thinned during the dehydrogenated process at a slightly lower laser intensity of 4 kW/cm^2, while the complete dehydrogenation is observed after annealing for 1.4 ms associated with a thickness shrinking from 280 nm to 240 nm. TEM analysis and photoluminescence spectroscopy at 806 nm reveal that the Si nanocrystals with maximum diameter and density of 5.3 nm and 10^{18} cm^{-3}, respectively, can be precipitated as the CO_2 laser intensity increase to an ablation threshold intensity of 5.8 kW/cm^2. The laser ablation introduces numerous structural defects and causes the anomalous absorption as well as photoluminescence at blue-green wavelengths in the $SiO_{1.25}$ film. From the reflection spectra with enlarged interfering fringe amplitude, the increasing refractive index (from 1.57 to 1.88) of the $SiO_{1.25}$ with increasing laser intensity can be concluded. In comparison with that of the quartz or as-grown sample, the red-shifted optical bandgap energy of the CO_2 laser-annealed $SiO_{1.25}$ film from 5.4 eV to 4 eV has evidenced the effect of the strong blue-green absorption on the oxygen vacancy defect. The forward turn-on voltage and current density of the ITO/CO_2 laser annealed SRSO/*p-Si*/Al MOS diode are 79 V and 33 μA/cm^2, respectively. The maximum output power of 29 nW associated with a P-I slope of 4.4 mW/A is determined.

Keywords: CO_2 laser annealing, Si nanocrystal, photoluminescence, electroluminescence, Si-rich SiO_x

1. INTRODUCTION

The synthesis of nanocrystallite silicon (nc-Si) embedded in the silicon-rich silicon oxide (SRSO) layer is a key process toward the demonstration of all-Si based light-emitting diodes (LEDs) and integrated-circuits (ICs)[1], which usually requires a long-term and high-temperature furnace annealing process (longer than 30 min)[2,3]. It is previously reported that the optimized photoluminescence (PL) and electroluminescence (EL) of a multirecipe Si-ion-implanted SRSO layer is acquired under the thermal annealing process at 1100°C for 3 hrs (ref. 4), whereas the optimized annealing condition for precipitating the nc-Si in a plasma-enhanced chemical-vapor deposition (PECVD)-grown SRSO film is 30 min at 1100°C (ref. 2). This approach meets the difficulty in its compatibility with the current IC fabricating procedure, as the high temperature environment over 500°C could seriously damage the ICs integrated with the SRSO based LEDs. In stead, the conventional approach is not applicable for annealing a specific area of the sample. Recently, the CO_2 laser based zone annealing approach has successfully utilized in the crystallization of the lead zirconate titanate material[5] and Mg-Doped GaN films[6]. It is know that the laser annealing techniques can be employed to modify the morphology or structural properties of different materials including metallic thin films[6-8], and dielectrics[9] etc. The premier demonstration on the synthesis of nc-Si embedded in the SRSO layer by using CO_2 laser annealing process has been

Nanophotonics, edited by David L. Andrews, Jean-Michel Nunzi, Andreas Ostendorf,
Proc. of SPIE Vol. 6195, 619515, (2006) · 0277-786X/06/$15 · doi: 10.1117/12.663184

Downloaded From: http://proceedings.spiedigitallibrary.org/ on 04/26/2014 Terms of Use: http://spiedl.org/terms

reported[10]. Based on the relatively large absorption coefficient as high as 1.2×10^3 cm^{-1} of the SiO_2 material at wavelength of 10.6 μm, the luminescent properties of the CO_2 laser annealed PECVD-grown SRSO layer on quartz substrates were investigated. In this work, the transmission and reflection spectroscopic analyses of CO_2-laser annealed SRSO layer are investigated. The variation on absorption coefficients and refractive indices of CO_2 laser dehydrogenated and ablated SRSO films are also characterized and elucidated. The analysis of optical and electrical properties between the CO_2 laser and furnace annealed SRSO layers is demonstrated. The experimental evidences and corresponding mechanisms of the defect- or nc-Si-related PL and EL from two metal-oxide-semiconductor (MOS) diodes fabricated on PECVD-grown SRSO/Si substrates are investigated, compared and elucidated in more detail.

2. EXPERIMENTAL SETUP

The SRSO layer was grown on the double-side polished quartz (GE, Type 219) substrates and p-type Si substrate by using a PECVD system at pressure of 120 mtorr a N_2O/SiH_4 fluence ratio of 6:1 under forward power of 45 W. The N_2O fluence was controlled at 120 sccm. The quartz and Si substrate temperature were hold at 150°C for 15 min to balance the substrate and chamber temperature before deposition. After deposition, a continuous-wave CO_2 laser (LTT Corp., ILS-II with a maximum power of 30 W) was used to perform the laser annealing process in atmosphere and the laser intensities was ranging from 1.5 to 13.5 kW/cm^2. The CO_2 laser annealing time was set as 1 ms. The laser spot of the CO_2 laser was focused within 0.2 mm^2 using a hemispherical lens, which can only be reduced to 130 μm^2 (limited by Rayleigh criterion, $D = 1.22\ \lambda/NA$, where D is the diameter of the spot, λ is the wavelength of the light source, and NA is the neutral aperture). The ablation thickness of the SRSO layer was measured by the α-step profiler or the atomic force microscope with a depth resolution of 1 nm. The PL of the laser-treated SRSO layer was excited by a He-Cd laser with an intensity of 5 W/cm^2 at the wavelength of 325 nm and was analyzed by a monochromator (Jobin Yvon, TRIAX-320) and a photomultiplier (Hamamatsu, R928). The diameter of the beam spot of the excitation laser and the CO_2 laser are about 30 μm and 500 μm, respectively. The spot size of the excitation laser is smaller.

During the PL measurement, the excitation laser beam spot was always focused at the center of the CO_2 annealed SRSO layer. The transmittance and reflectance of the samples were measured over the wavelength range between 190 nm and 850 nm (with 0.1 nm resolution) using a commercial UV-VIS transmission and reflection spectrophotometer (Shimadzu, UV-2401PC). The wavelength accuracy of the measurement system was confirmed by using an 850-nm laser diode. An HRTEM (JEOL, 4000EX TEM) with a point-to-point resolution of 0.17 nm was used to characterize the orientation, the lattice spacing, the size, and the density of the precipitated nc-Si in the SRSO layer. The composition of the SRSO layer on the Si substrate has been analyzed by using Rutherford Backscattering Spectrometry (RBS) measurement, which bombards the SRSO layer with 2 MeV He^+-ions and picks up the backscattering signal at an angle of 170°. The composition of the SRSO layer was analyzed using commercial software "Rump". To characterize the EL response, the samples after CO_2 laser and furnace-annealing were diced to 1mm×1mm square and were evaporated with an ITO (on the top of SRSO) film to form the metal-oxide-semiconductor (MOS) diodes. The contact thickness and diameters were set as 2000Å and 0.8 mm, respectively. A 5000-Å Al contact electrode was coated on the bottom of the Si substrate.

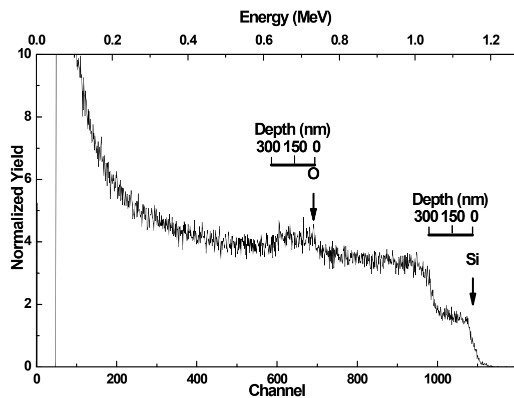

Fig. 1: RBS spectrum of the as-grown $SiO_{1.25}$ film on a Si substrate.

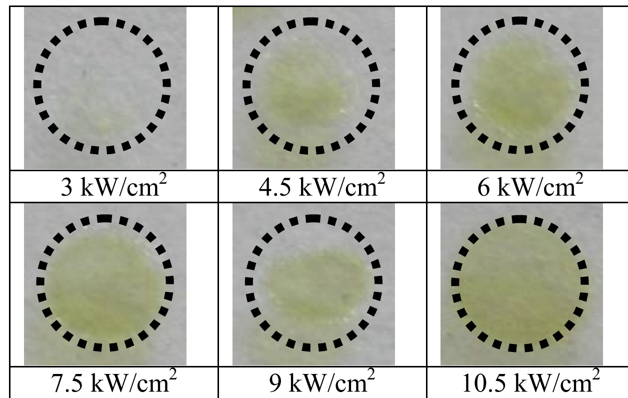

Fig. 2: Far-field patterns of SRSO layers after the laser annealing at increasing P_{laser} from 3 to 10.5 kW/cm^2.

3. RESULT AND DISCUSSION

Downloaded From: http://proceedings.spiedigitallibrary.org/ on 04/26/2014 Terms of Use: http://spiedl.org/terms

3.1 Material aspects of the CO_2 laser annealed silicon-rich dioxide ($SiO_{1.25}$) layer

The RBS spectrum of the SRSO layer on the Si substrate indicates clear signals of Si and oxygen at 1.147 MeV and 742.0 keV, respectively, as sown in Fig. 1. It reveals that the thickness of the as-deposited SRSO layer is about 280 nm, which is in good agreement with that measured by a surface profiler. The calculated ratio of O/Si in the SRSO layer is 1.25. The Si concentration of the $SiO_{1.25}$ is 44.44 atomic %, which is calculated on RBS measurement results of the $SiO_{1.25}$ film. Since the Si concentration of the SiO_2 film is 33.33 atomic %, the excess Si concentration of the $SiO_{1.25}$ film is determined as 11.11 atomic %. The precise control on the output power of the CO_2 laser causes a fine adjustment of annealing temperatures on the SRSO layer. The CO_2 laser annealing acquires the annealing time of only 1 ms for precipitating nc-Si, which is shorter than that required in a furnace-annealing process. The CO_2 laser beam can tightly focused into a spot size of ~10 μm, which can be position-controlled by using a programmable X-Y translation stage. Therefore, advantages of the CO_2 laser based rapid-thermal-annealing process are its in-situ, localized and two-dimensional treatment. For a SRSO layer deposited on the polished quartz, the CO_2 laser annealing region turns the color from light-yellow to dark-yellow with the increasing P_{laser} from 3 to 10.5 kW/cm^2 (see Fig. 2).

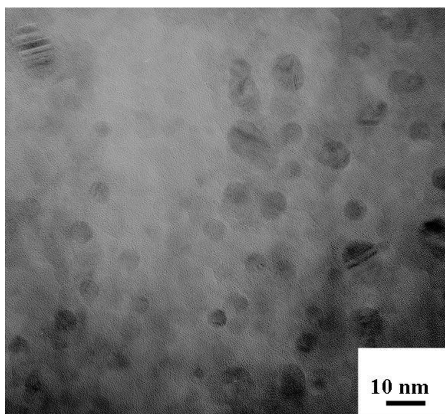

Fig. 3: Planar-HRTEM photograph of the $SiO_{1.25}$ film annealed at P_{laser} = 5.8 kW/cm^2.

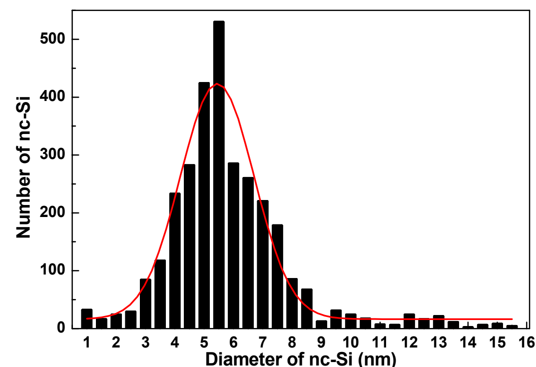

Fig. 4: The size distribution of the Si nanocrystal in the $SiO_{1.25}$ film annealed at P_{laser} = 5.8 kW/cm^2.

The surface density of Si nanocrystals buried in $SiO_{1.25}$ film annealed at P_{laser} = 5.8 kW/cm^2 was calculated from the planar photograph of $SiO_{1.25}$ film taken by HRTEM, as shown in Fig. 3. The estimated number of the Si nanocrystal in the area of 1.21×10^{-10} cm^2 is about 3132. Therefore, the surface density of Si nanocrystals was estimated about 2.6×10^{13} cm^{-2}. An average size of 5.3 nm can be estimated by a size-distribution bar chart of the Si nanocrystal, as shown in Fig. 4. The thickness of $SiO_{1.25}$ after the dewas further determined as 220 nm by a cross-sectional HRTEM of the $SiO_{1.25}$ film. The volume density ρ of Si nanocrystals buried in CO_2 laser annealed $SiO_{1.25}$ film is 1.1×10^{18} cm^{-3} as estimated from planar and cross-sectional HRTEM images. The Si concentration of the $SiO_{1.25}$ is 44.44 atomic %, which is calculated on RBS measurement results of the $SiO_{1.25}$ film. Since the Si concentration of the SiO_2 film is 33.33 atomic %, the excess Si concentration of the $SiO_{1.25}$ film is determined as 11.11 atomic %. Since the Si exhibits a diamond lattice structure that consists of eight atoms in a unit cell. Taking the Si lattice constant of 0.543 nm, the number of Si atoms per cubic centimeter of $8/a^3 = 8/(5.43\times10^{-8})^3 = 5\times10^{22}$ atoms/cm^3 can be obtained. The estimated average diameter and volume of the buried nc-Si are about 5.2 nm and 7.79×10^{-20} cm^3, respectively. In this case, such an nc-Si is constructed by 3897 Si atoms (N = 7.79×10^{-20} cm^3 × 5×10^{22} atoms/cm^3 =3897 atoms). Since the density of the PECVD-grown SiO_2 is 1.4 g/cm^3. Therefore, the number of Si atom per cubic centimeter in the PECVD-grown SiO_2 is about 1.4×10^{22} atoms/cm^3, as calculated by

$$(6.0221\times10^{23}\, atoms/mol\times1.4 g/cm^3)/(60\ g/mol)=1.4051\times10^{22}\, atoms/cm^3$$

The atomic mass of the $SiO_{1.25}$ becomes 48 amu, and the evaluated density of $SiO_{1.25}$ is 1.95 g/cm^3, which is linearly interpolated the density of SiO material (D_{SiO} = 2.13 g/cm^3). The number of Si atom per cubic centimeter of the PECVD-grown $SiO_{1.25}$ film is calculated as 2.45×10^{22} atoms/cm^3.

$$6.0221\times10^{23}\ atoms/mol\times1.95\ g/cm^3/(48\,g/mol)=2.4465\times10^{22}\, atoms/cm^3$$

Consequently, the number of the 11.11 atomic % of excess Si atoms buried in the $SiO_{1.25}$ film in our experiment is about 1.04132146×10^{22} atoms/cm^3.

Downloaded From: http://proceedings.spiedigitallibrary.org/ on 04/26/2014 Terms of Use: http://spiedl.org/terms

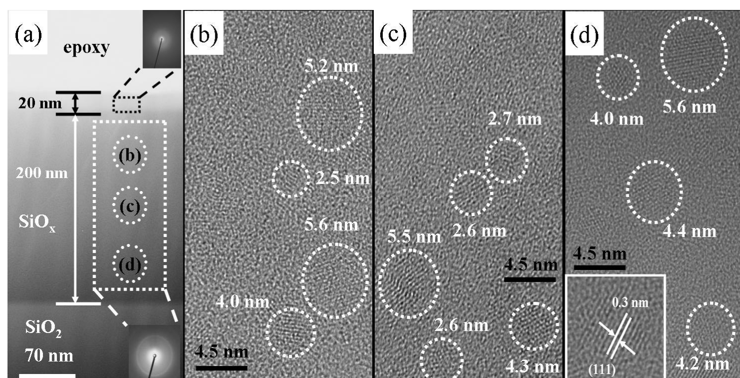

Figure 5: Cross-sectional HRTEM images of CO_2-laser-annealed SRSO at P_{laser} = 6 kW/cm^2. Inset: the electron diffraction pattern (lower left) of a (111)-plane Si nanocrystal (lower right).

In more detail, there are three layers observed from the cross-sectional HRTEM image of a thicker SRSO sample, as shown in Fig. 5(a), including an epoxy layer (upper), a SRSO layer (middle) and a pure quartz layer (lower). The cross-sectional HRTEM image reveals that the size distribution of the nc-Si embedded in a SRSO layer, see Fig. 2(a)-2(c), is almost the same, which indicates that the vertical temperature distribution in the depth of 220 nm is uniform. Moreover, the cross-sectional HRTEM image in Fig. 5 reveals that the orientation of nc-Si precipitated in the laser annealed SRSO layer is random, which is due to the diffractive pattern of the area with nc-Si is a ring pattern, as shown in Fig. 5(a). For one of the nc-Si, its phase structure is crystal phase, as shown in Fig. 5(b)-5(d), which can be confirmed by the lattice space of Si material. Several plane orientations can be obtained, as shown in the inset of Fig. 5(d), such as (110), (111), (002) and (021) planes with the plane spaces of 0.38 nm, 0.31 nm, 0.27 nm and 0.24 nm, respectively. The plan-view HRTEM indicates the maximum volume density of the nc-Si in SRSO layer annealed at 5.8 kW/cm^2 is up to 1.1×10^{18} cm^{-3}, which is in good agreement with the theoretically estimated density of 2.7×10^{18} cm^{-3} under the assumption on the nc-Si diameter of 5.3 nm (containing nearly 3900 Si atoms).

3.2 Transmission and reflection spectroscopy of CO_2 laser annealed $SiO_{1.25}$

The change in color of the SRSO layer is mainly attributed to the variation of both the absorption coefficient and due to the precipitation of nc-Si embedded in the SRSO layer. The transmission spectra of the as-grown and CO_2 laser-treated SRSO samples in the near infrared region show a similar transparent result with transmission coefficient of over 85 % as reported previously[11-12], as shown in Fig. 6.

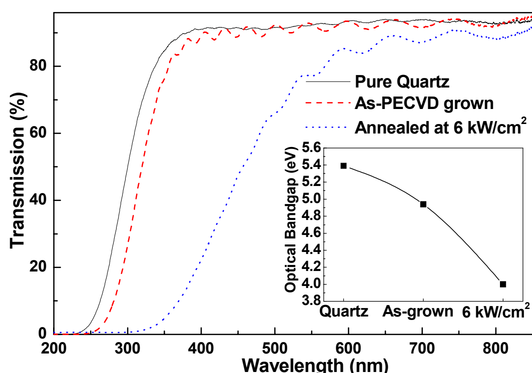

Fig. 6: Transmission spectra of pure quartz, as-PECVD grown $SiO_{1.25}$ film and laser-treated $SiO_{1.25}$ film at P_{laser} of 6 kW/cm^2.

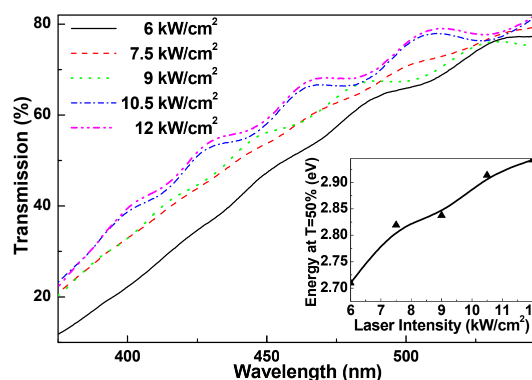

Fig. 7: Transmission spectra of laser-treated $SiO_{1.25}$ films at P_{laser} from 6 to 12 kW/cm^2.

The absence of the near-infrared absorption in laser-treated SRSO samples indicates a small absorption cross-section or density of the nc-Si. Nonetheless, a slight red-shift on the transmission band-edge of the as-grown sample as compared to that of the pure quartz, corresponding to a shrinking optical bandgap of the $SiO_{1.25}$ film from 5.4 eV to 4.9 eV (see inset of Fig. 6). This is elucidated by the increasing oxygen non-bonding electronic states in $SiO_{1.25}$ near the

Downloaded From: http://proceedings.spiedigitallibrary.org/ on 04/26/2014 Terms of Use: http://spiedl.org/terms

valence band-edge[13]. The valence band-edge moves up and the conduction edge simultaneously moves down as the Si-rich condition becomes significant, while the increased Si–Si bond states are gradually overlaid with the oxygen non-bonding states and finally spread out into the Si valence band. The net result is that the bandgap decreases nonlinearly when Si concentration continually increases.

The interfered fringe occurred between 350 nm and 750 nm interprets the different refractive indexes of the SRSO layer and pure quartz substrate, which is attributed to the 11 atomic % of excess Si atoms in the $SiO_{1.25}$ film. After the CO_2 laser annealing at P_{laser} = 6 kW/cm^2, the laser-annealed $SiO_{1.25}$ sample shows a stronger absorption between 400 nm and 600 nm than that of the as-PECVD grown sample or pure quartz. In comparison with the transmission spectra of the as-grown and laser-treated samples, a clear absorption spectrum between 350 nm and 600 nm was observed, and the optical bandgap of the laser-annealed $SiO_{1.25}$ film in comparison with that of the as-grown $SiO_{1.25}$ film redshifts from 4.9 eV to 4 eV, see the inset of Fig. 6. Several possibilities may be considerable to red-shift the transmission spectrum band-edge of the laser-annealed $SiO_{1.25}$ film, such as the oxygen related defects and the different composition of the SRSO layer. The red-shift transmission spectrum is not attributed to the nc-Si, however, which coincides well with the defect related blue-green PL spectrum of the laser-treated SRSO layer at the P_{laser} >6 kW/cm^2. It is obvious that the red-shifted transmission spectrum was attributed to the absorption of the NOV and weak-oxygen-bond defects due to the overlapping emission and absorption spectra. At larger annealed laser intensities from 6 to 12 kW/cm^2, the transmission spectra of SRSO samples illustrate blue-shifted phenomenon from 456.6 nm to 422.4 nm at the transmission of 50 %, as shown in Fig. 7. In particular, the transmission at the wavelength of 410 nm increases from 27 % for the P_{laser} of 6 kW/cm^2 to 43 % for the P_{laser} of 12 kW/cm^2, which corresponds to the decreasing thickness of the SRSO layer after CO_2 laser ablation.

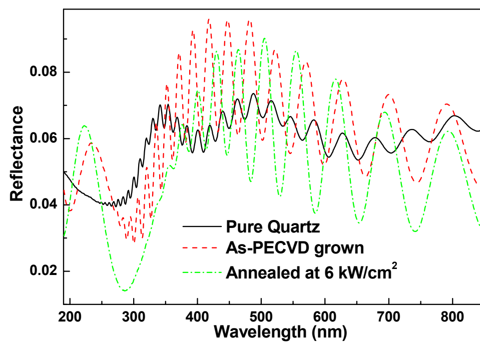

Fig. 8: Reflectance spectra of Quartz, as-PECVD grown $SiO_{1.25}$ film and the CO_2 laser annealed $SiO_{1.25}$ film at P_{laser} = 6 kW/cm^2.

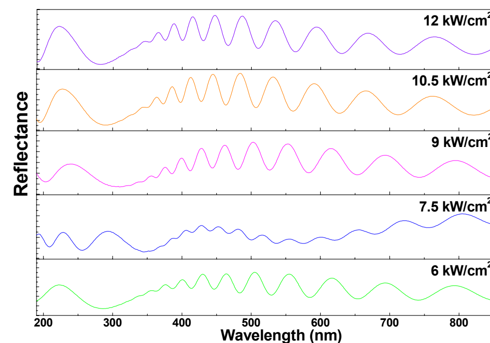

Fig. 9: Reflectance spectra of CO_2 laser annealed $SiO_{1.25}$ films at P_{laser} increasing from 6 to 12 kW/cm^2.

In addition, the reflection spectra of the laser-treated $SiO_{1.25}$ film show a strongly interfered fringe as compared to that of the pure or as-grown $SiO_{1.25}$ film, as shown in Fig. 8. The precipitation of nc-Si embedded in the SRSO layer causes the increasing refractive index of the SRSO layer. The almost same reflection patterns of laser-treated $SiO_{1.25}$ films at the laser intensities over 6 kW/cm^2 reveal that the refractive indexes of laser-treated $SiO_{1.25}$ films remain unchanged, as shown in Fig. 9. Since the excess Si in the $SiO_{1.25}$ film is 11 % and constant for the CO_2 laser annealing duration, the precipitation density of nc-Si will be saturated at a certain laser annealing intensity and beyond. According to the reflection fringes in Fig. 9, the refractive indexes of laser-treated $SiO_{1.25}$ films as a function of annealing laser intensities are calculated and shown in Fig. 7 by using the fringe contrast formula that defines the ratio of maximum to minimum reflectance, as given by[14]

$$R(\max)\big/R(\min) = \left[(R_1 + R_2)(1-\sqrt{R_1R_2})^2\right]\Big/\left[(1+R_1R_2)(\sqrt{R_1}-\sqrt{R_2})^2\right]. \quad (1)$$

To confirm, a Bruggeman effective-medium approximation (BEMA)[15,16] simulation is also used to estimate the refractive index of the CO_2 laser annealed $SiO_{1.25}$ film at the P_{laser} of 6 kW/cm^2. Assuming that the composite material exhibits two phases with volume fractions f and $1-f$, respectively. The effective complex dielectric function can be calculated by

$$f_{nc-Si}[(\varepsilon_{nc-Si} - \varepsilon_{SiO_{1.25}})/(\varepsilon_{nc-Si} + 2\varepsilon_{SiO_{1.25}})] + f_{SiO_2}[(\varepsilon_{SiO_2} - \varepsilon_{SiO_{1.25}})/(\varepsilon_{SiO_2} + 2\varepsilon_{SiO_{1.25}})] = 0 \quad (2)$$

Downloaded From: http://proceedings.spiedigitallibrary.org/ on 04/26/2014 Terms of Use: http://spiedl.org/terms

where $f_{nc\text{-}Si} + f_{SiO2} = 1$, $\varepsilon_{nc\text{-}Si}$, $\varepsilon_{SiO1.25}$, and ε_{SiO2} are the dielectric functions of the nc-Si, the laser-treated Si-rich $SiO_{1.25}$ film, and the SiO_2 film, respectively. With the nc-Si density of 1.1×10^{18} cm^{-3}, the estimated refractive index of the laser-treated $SiO_{1.25}$ film at the P_{laser} of 6 kW/cm^2 is about 1.82 at the wavelength of 633 nm, which is close to the result in Fig. 10 obtained from reflection spectra. Similar refractive index of a thermally annealed Si^+ implanted SiO_2 was also reported by En Naciri *et al*. [17]. At a surface temperature below 600°C (or P_{laser} <3 kW/cm^2), the change in refractive index of the CO_2 laser-annealed SRSO layer is less than 0.6 % since the precipitation of nc-Si has not been initiated yet. The refractive index of SRSO layer increases from 1.69 to 1.88 as the annealing temperature increases from 900 to 1300°C. That is, the nc-Si precipitation becomes more pronounced at the larger CO_2 P_{laser}. In previous studies, Prakash *et al*.[18] have measured refractive indices of 1100°C annealed PECVD-grown SRSO layers with total Si concentrations of 39 atomic %, 42 atomic % and 46 atomic % are 1.84, 1.93 and 2.15, respectively. Later on, Khriachtchev *et al*.[19] have also reported that the refractive index increases with the excess Si concentration, in which the refractive indices of the 1150°C annealed Si-rich SiO_x samples with x = 1.85, 1.57 and 1.45 are 1.65, 1.8 and 1.9, respectively. Moreover, En Naciri *et al*.[17] also observed that the refractive index of a SiO_2 film can be increased up to 2.3 at 633 nm after implanting with Si ions at a fluence of 8×10^{18} cm^{-2} at substrate temperature of 500°C and annealing at 1100°C for 2 hrs. All of the aforementioned results strongly corroborate increasing refractive index of a thermally annealed SRSO layer under the precipitation of nc-Si. The density of the nc-Si film significantly enlarges as the excess Si concentration of the SRSO layer increases. The tiny change in refractive index of the laser-treated $SiO_{1.25}$ film at the P_{laser} of 12 kW/cm^2 is attributed to the oxidation of outer nc-Si.

3.3 The dehydrogenation and ablation of CO_2 laser annealed $SiO_{1.25}$

Note that since the as-grown SRSO layer contains a high concentration of hydrogen, a pre-annealing process is used to obtain a hydrogen-free, compact SRSO layer owing to the loss of hydrogen during the annealing action. To distinguish the shrinkage of the SRSO layer thickness either by the CO_2 laser annealing induced de-hydrogenation or by CO_2 laser ablation process, the SRSO sample was first de-hydrogenated by annealing either in a furnace at 1100°C or with a CO_2 laser at intensity of 4 kW/cm^2 (well below ablation threshold). The thicknesses of annealed SRSO layers are plotted as a function of annealing time, as shown in the Fig. 11. The de-hydrogenating process is finished after furnace annealing at 1100°C for three hrs, while the thickness of the annealed SRSO layer reduces from 281 nm to 242 nm. A similar result is also observed in the CO_2 laser annealed SRSO sample after illuminating for 1.4 ms or longer. The shrinking depth of the PECVD-grown SRSO layer during annealing is about 38-39 nm. Since a PECVD-grown SRSO layer contains high concentrations of hydrogen, the loss of hydrogen during annealing is attributed to the compaction of the SRSO layer. Afterwards, the CO_2 laser ablation experiment was performed using the de-hydrogenated SRSO layer with thickness of about 240 nm. This is done by illuminating the SRSO sample in atmosphere with a CO_2 laser at different intensities (ranging from 1.5 to 13.5 kW/cm^2). The ablation depth of the SRSO layer was measured as a function of the P_{laser} ranging from 1.5 to 13.5 kW/cm^2, as shown in Fig. 12. A linear ablation slope of 29 nm/ (kW/cm^2) was observed at P_{laser} > 6 kW/cm^2.

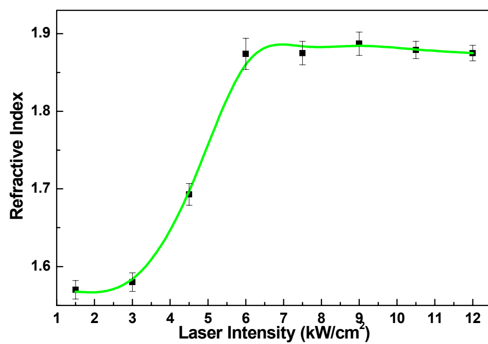

Fig. 10: Refractive index of CO_2 laser annealed $SiO_{1.25}$ film as a function of P_{laser}.

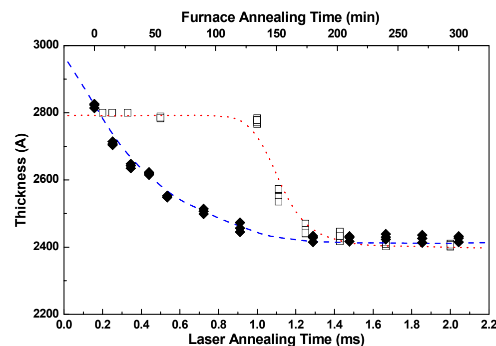

Fig. 11: The thicknesses of annealed $SiO_{1.25}$ films as a function of annealing time.

In previous studies[20], an ArF pulse excimer laser at the wavelength of 193 nm was first used to evaporate SiO powder with an energy deposition of 110 mJ/cm^2 per pulse, which is generally a laser sputtering process although a Si-SiO_2 phase separation was observed. Rossi *et al*.[21] proposed the formation of nc-Si with diameters of 2.5 to 12 nm embedded

Downloaded From: http://proceedings.spiedigitallibrary.org/ on 04/26/2014 Terms of Use: http://spiedl.org/terms

in the undoped amorphous silicon oxide (a-SiO_x:H) layer containing different oxygen content of 28, 35 and 40 % by using continuous-wave (CW) Ar^+ laser (λ=514.5 nm) treatment at the intensity of 10^5 W/cm^2. In their experiment, the required Ar^+ laser intensity is much higher than that our condition using a CO_2 laser, which is mainly due to the relatively small absorption coefficient of 1×10^{-6} cm^{-1} of the SiO_2 material at wavelength of 514.5 nm. The surface temperature is linear proportional to the absorption coefficient, however, the absorption coefficient of the SiO_2 layer at wavelength from 200 nm to 3000 nm is much lower than that at 10.6 μm.[22] Even though a pulsed Nd:YAG laser (τ=8 ns, λ=355 nm) or KrF excimer laser[23,24] (λ=248 nm) was employed to synthesize nc-Si in Si-rich oxide matrix with least laser intensity of 30-85 mJ/cm^2, the pulse intensity of 4-10 MW/cm^2 is still far beyond the laser ablation threshold. Such a low absorption coefficient at aforementioned wavelength range is unavailable to achieve enough temperature for synthesizing nc-Si at laser intensity below ablation threshold of 6 kW/cm^2. That is, the structural damage is associated with the high-power annealing process, which usually introduces other defects related effects in the oxide materials.

In PL analysis, a broadband blue-green PL was observed in the SRSO film after CO_2 laser annealing at the intensity of 1.5 kW/cm^2, as shown in Fig. 12(a). One of the decomposed peaks at 520 nm with 225nm linewidth is attributed to the E'$_\delta$ defect (a precursor of nc-Si, denoted as [Si↑Si—Si])[25], and the other at 455 nm with 115nm linewidth is contributed by the neutral oxygen vacancy (NOV, denoted as [O_3≡Si-Si≡O_3]) center[21,22]. As the laser annealing intensity increases, the blue-green PL corresponding to the E'$_\delta$ center and NOV defect were enhanced associated with narrowing linewidths of 176 nm and 99 nm, respectively. Afterwards, the PL peak red-shifts to 520 nm as P_{laser} slightly increases to 3 kW/cm^2 (equivalent to a surface temperature of 900°C), indicating a more pronounced activation of the E'$_\delta$ defects than the NOV defects. This phenomenon is somewhat similar to that ever observed in a furnace-annealed SRSO layer, as shown in Fig. 12(b). In comparison with the previous studies[25,26], the optimized furnace annealing time for the E'$_\delta$ defect is >4 hrs at temperature of 1100°C, which is much longer than that of the CO_2 laser annealing process.

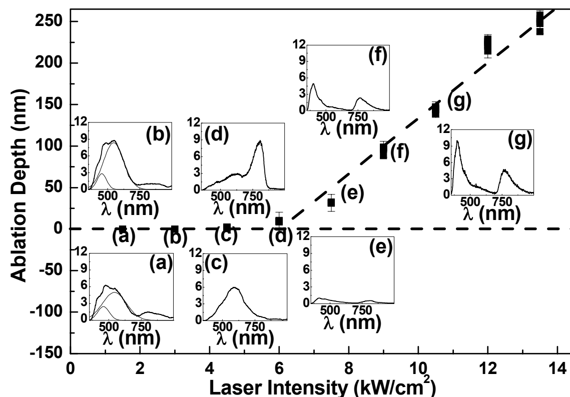

Fig. 12: CO_2 laser ablation thickness as a function of the laser intensity. Inset: PL spectra of laser-treated $SiO_{1.25}$ films at the P_{laser} of (a)1.5 (b)3 (c)4.5 (d)6 (e)7.5 (f)9 (g)10.5 kW/cm^2.

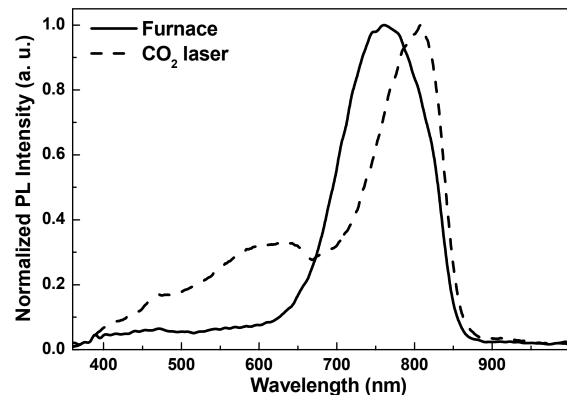

Figure 13: PL spectra of the furnace annealed (solid line) and CO_2 laser annealed (dash line) samples.

It is seen in Fig. 12(c) that the PL further red-shifts to the wavelength of 600-620 nm as the P_{laser} is increased to 4.5 kW/cm^2, indicating a diminish of NOV and other structural defects and the increasing density of small-size nc-Si precipitated from E'$_\delta$ defects. A significant PL peak at 806 nm with 100nm linewidth is observed at P_{laser} of 5.8 kW/cm^2, as shown in Fig. 12(d), such an optimized annealing intensity of the nc-Si in the SRSO layer is near the ablation threshold. In addition, a high-intensity CO_2 laser annealing not only locally anneals the SRSO layer for nc-Si precipitation but also introduces structural defects with PL at 400-600 nm nearby the nc-Si in such a short-term heat treatment. These defects are mostly oxygen dependent and some of them are the NOV defects originate from the nc-Si precipitation process as most of the excessive Si atoms occupied the sites of oxygen move away to precipitate nc-Si. The precipitated nc-Si inevitably compresses the SRSO matrix and results in the formation of interstitial oxygen dependent new defects, such as the weak-oxygen bond or ionized oxygen molecule (O_2^-)[23,24] at PL wavelength of 410 nm, as shown in Fig. 12(e)-(g). After SRSO samples were laser-annealed at the optimum P_{laser} = 6 kW/cm^2 and furnace-annealed at 1100°C for the optimum annealing time of 30 min, the peak wavelength of the PL spectrum from the laser-annealed sample is longer than that from the furnace-annealed sample with the offset value of 46 nm, as shown in

Downloaded From: http://proceedings.spiedigitallibrary.org/ on 04/26/2014 Terms of Use: http://spiedl.org/terms

Fig. 13, which is attributed to the average size of nc-Si buried in the laser-annealed sample is larger than that of furnace-annealed sample. Note that PL intensity of the laser-annealed sample from the wavelength of 400 nm to 650 nm is higher than that of the furnace-annealed sample, which is due to the existence of oxygen-related defects in the laser-annealed sample, such as weak-oxygen-vacancy, NOV, NBOHC or E'_δ defect. Since the CO_2 rapid-laser-annealing process is complete at the duration of 1ms, oxygen or Si atoms do not suffer from an enough time to remove away or precipitate into nc-Si. However, such a phenomenon was never observed in the furnace annealed sample since the high-temperature and long-term furnace annealing usually causes a gradual recovery on the compressing strain of the SiO_2 matrix nearby the nc-Si. On the other hand, the slight red-shift of the PL peak wavelength from 806 to 825 nm indicates an increase in size of the nc-Si as the P_{laser} increases further from 6 to 7.5 kW/cm^2. This result correlates well with previous observations[25] that the PL red-shifts from 700 nm to 950 nm as furnace temperature increases from 1100°C to 1250°C. However, the ablation of the SRSO layer occurring at such high P_{laser} also leads to another featured PL at 410 nm due to structural damage, as shown in Fig. 12(f). This results in a concurrent decrease in the near-infrared PL intensity by an order of magnitude, whereas the intensity of blue PL at 410 nm varies oppositely. In fact, the 410-nm PL intensity is increased by one order of magnitude as the P_{laser} increases from 7.5 to 11 kW/cm^2, while the surface temperature has already exceeded the melting temperature of fused silica.

3.5 EL and I-V of PECVD-grown SRSO based MOS diode

The I-V and P-I responses of the MOS diodes made on CO_2 laser-annealed and 30-min furnace-annealed PECVD-grown SRSO layers are shown in Fig. 14. A $SiO_{1.25}$ layer on the *p-Si* substrate was laser-annealed at P_{laser} = 6 kW/cm^2 or furnace-annealed at 1100°C for 30 min. For the ITO/CO_2 laser annealed SRSO/*p-Si*/Al MOS diode, the forward turn-on voltage and current density are 79 V and 33 μA/cm^2, respectively. The maximum output power of 29 nW associated with a P-I slope of 4.4 mW/A is determined. For the ITO/ furnace annealed SRSO/*p-Si*/Al MOS diode, the forward turn-on voltage and current density are 87 V and 116 μA/cm^2, respectively. The maximum output power of 15.5 nW associated with a P-I slope of 3.4 mW/A is determined. The tunneling based carrier transport mechanism is dominated due to the exponential-like I-V behavior.

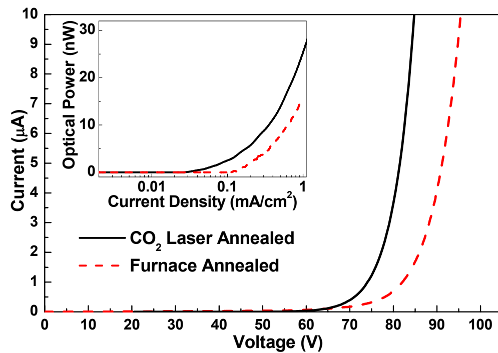

Fig. 14: P-I (Inset) and I-V responses of the CO_2 laser (solid line) and furnace-annealed (dash line) ITO/SRSO/*p*-Si/Al MOS diodes.

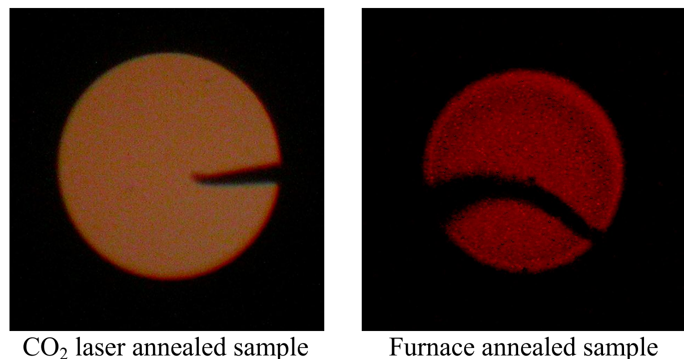

Fig. 15: Far-field EL pattern of the ITO/CO_2 laser annealed SRSO/*p-Si*/Al and ITO/furnace annealed SRSO/*p-Si*/Al MOS diodes biased at 80 V and 90 V, respectively.

The furnace annealed sample shows a higher turn-on voltage as compared to the CO_2 laser annealed sample, which is attributed to the fewer non-radiated and irradiated defects within furnace annealed PECVD-grown SRSO material. A better crystallinity of the PECVD-grown SRSO film makes the current hard to tunneling through, which has also been corroborated by the lack of structural damage (WOB and NOV defects) related PL and EL signal at blue-green region. The far-field patterns of the ITO/CO_2 laser annealed SRSO/*p-Si*/Al and ITO/furnace annealed SRSO/*p-Si*/Al MOS diodes at forward bias 80 V and 90 V, respectively, are shown in Fig. 15. The EL spectrum of furnace annealed PECVD-grown SRSO based ITO/SRSO/Si/Al MOS diode sample is shown in Fig. 16, which is decomposed into dual luminescent peaks at wavelengths of 625 and 768 nm with spectral linewidths of 189 nm and 154 nm, respectively. Note that the EL components at longer wavelength coincides well with that of PL, which reveals that the nc-Si related PL and EL are attributed to the same carrier recombination mechanism in the buried nc-Si. Franzo *et al.*[31] have attributed the EL at 700-850 nm to the impact ionization and recombination in buried nc-Si. More important, Irrera *et al.*[32] clarified that the impact ionized carriers are confined and recombined within the nc-Si without accelerating under

Downloaded From: http://proceedings.spiedigitallibrary.org/ on 04/26/2014 Terms of Use: http://spiedl.org/terms

the high electric field. De La Torre *et al.*[33] found a very weak temperature dependence on the I-V response of the Al/SRSO:nc-Si/p^+-Si LED with a 40-nm thick SiO_2 film, which is relatively in agreement with the tunneling conduction process. Our results indicates that the Fowler-Nordheim (F-N) process is not occurred due to a low electric field of <5 MV/cm. It is thus concluded that the carriers in nc-Si is neither thermally activated or field-enhanced F-N tunneling injected, but is possibly assisted by direct tunneling between nc-Sis.[32]

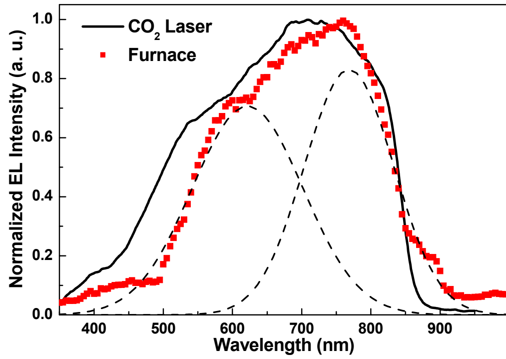

Fig. 16: Normalized EL spectra of the ITO/CO_2 laser annealed SRSO/*p-Si*/Al (solid) and ITO/furnace annealed SRSO/*p-Si*/Al (square dotted) MOS diodes biased at 80 V and 90 V, respectively. The decomposed EL components at 625 nm and 768 nm are shown (dashed).

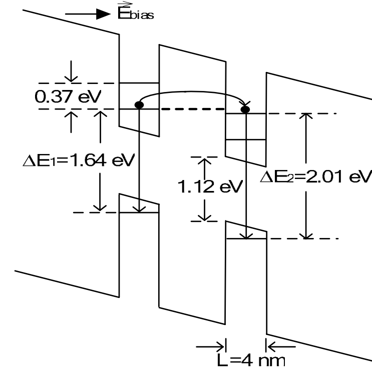

Fig. 17: The cold-carrier tunneling mechanism happened in high-excited states between adjacent nc-Si quantum dots in the ITO/SRSO/p-Si/Al MOS structure.

However, the mechanism of secondary EL peak expanded to shorter wavelength region (500-700 nm) is yet unclear. Previously, Franzo *et al.*[26] suggested that the blue-shifting EL is mainly due to the impact excitation of smaller nc-Si (emitting at shorter wavelength) by the injected carriers with increasing energies under high biased condition. Even though, the effect of oxygen related defects on the secondary EL at about 660 nm was ever considered. De La Torre *et al.*[33] also attributed the 540-690nm EL to the preexisting defects in the SiO_2 matrix. Similar EL side-peak at 650 nm was discovered by Linnros and co-workers.[34] Up to now, no further explanations are addressed on the enhancement of short-wavelength EL under electrical instead of optical pumping process. Nonetheless, a possible cold carrier tunneling process was considered to happen in the ITO/SRSO/Si/Al MOS diode under appropriate bias.[35] Since the band structure of SRSO is seriously bending under extremely high electric field, the electrons could tunnel from a first-order quantized state (n=1) in one nc-Si to a second-order quantized state (n=2) in the adjacent nc-Si, as illustrated in Fig. 17. This provides a higher population in the second-order (n=2) state as well as an enhanced spontaneous emission at larger energy. According to the theory of quantum combined systems,[35,36] the band-to-band transition energies of first-order and second-order excited states for an nc-Si quantum dot with diameter of 4 nm are calculated as $\Delta E_1 = 1.64$ eV (or $\lambda_1 = 756$ nm) and $\Delta E_2 = 2.01$ eV (or $\lambda_2 = 616$ nm), respectively. These values exactly coincides with the wavelength of the EL components decomposed from our experimental results, the energy difference between two transitions are theoretically calculated as $\Delta E_{l=2\rightarrow l=1} = 3\pi^2\hbar^2/2m_e^*L^2 = 0.37 \pm 0.01$ eV, where l, m_e^* and L denote the angular momentum state, the electron effective mass and the diameter of nc-Si quantum dot, respectively.[41] In contrast, there is no significant PL contributed by the second-order states as compared to that contributed by first-order states in viewing of previous reports, which could be attributed to the absence of band-filling effect under such a low pumping density in PL measurements. The second-order state related PL is detectable as the first-order states are fulfilled by increasing the pumping flux density of photons. These observations primarily elucidate that the bias-dependent and blue-shifted EL is mainly attributed to the cold-carrier tunneling induced high-excited state transition effect between adjacent nc-Si quantum dots under a sufficiently high electric field.

4. CONCLUSSION

Electroluminescence of the CO_2 laser annealed PECVD-grown SRSO based MOS diode with embedded nc-Si is demonstrated. The structural and optical aspects of the localized synthesized Si nanocrystals in Si-rich $SiO_{1.25}$ film

Downloaded From: http://proceedings.spiedigitallibrary.org/ on 04/26/2014 Terms of Use: http://spiedl.org/terms

using CO_2 laser rapid thermal annealing at nearly ablation threshold P_{laser} = 5.8 kW/cm^2 is also characterized. The thickness of $SiO_{1.25}$ film was thinned from 280 to 240 nm during the dehydrogenating process at P_{laser} = 4 kW/cm^2 for 1.4 ms. After CO_2 laser annealing at P_{laser} from 1.5 to 13.5 kW/cm^2, the color of a $SiO_{1.25}$ film changes from light yellow to dark yellow is due to both the increasing absorption coefficient and refractive index of $SiO_{1.25}$ film. HRTEM analysis reveals the aveage diameter and density of 5.3 μm and 1.1×10^{18} cm^{-3}, respectively, for the precipitated Si nanocrystals in annealed SRSO film. The Si nanocrystal dependent PL were observed at 806 nm or longer, whereas the CO_2 laser ablation at P_{laser} > 6 kW/cm^2 damages the $SiO_{1.25}$ film and induces significant blue PL at 410 nm by oxygen-related structural defects. The refractive index of $SiO_{1.25}$ changes from 1.57 to 1.9 with increasing P_{laser} as calculated from the reflection spectra with an enlarged interference fringe amplitude. In comparison with that of Quartz or an as-grown sample, the red-shifted optical bandgap energy of a CO_2 laser annealed $SiO_{1.25}$ film from 5.39 to 4.0 eV has evidenced the effect of oxygen vacancy defect on the strong blue-green absorption. The forward turn-on voltage and current density of the ITO/CO_2 laser annealed SRSO/*p-Si*/Al MOS diode are 79 V and 33 μA/cm^2, respectively. The maximum output power of 29 nW associated with a P-I slope of 4.4 mW/A is determined. For the ITO/ furnace annealed SRSO/*p-Si*/Al MOS diode, the forward turn-on voltage and current density are 87 V and 116 μA/cm^2, respectively. The maximum output power of 15.5 nW associated with a P-I slope of 3.4 mW/A is determined. The EL of the ITO/furnace annealed SRSO/*p-Si*/Al MOS diode is mainly due to the transfer of cold carriers by direct tunneling between adjacent nc-Sis. The cold-carrier tunneling process from lower excited state to higher excited state between two adjacent nc-Si quantum dots under high electric field is primarily elucidated. The difference between PL and EL results is also explained with the proposed mechanism.

ACKNOWLEDGEMENT

This work was supported in part by National Science Council under grant NSC94-2215-E-009-040 and by Asian Office of Aerospace Research & Development (AOARD), the Detachment 2 of the Air Force Office of Scientific Research (AFOSR), under Contract No. FA5209-05-P-0626 AOARD 05-93.

REFERENCE

1. N. Lalic, J. Linnros, J. Lumines. **80**, 263 (1999).
2. G.-R. Lin, K. C. Yu, C. J. Lin, H. C. Kuo, M. C. Ou-Yang, Appl. Phys. Lett. **85**, 1000 (2004).
3. G.-R. Lin, C. J. Lin, C. K. Lin, L. J. Chou, Y. L. Chueh, J. Appl. Phys. **97**, 094306(2005).
4. G.-R. Lin, C. J. Lin, C. K. Lin, Appl. Phys. Lett. **85**, 935 (2004).
5. C. F. Chou, H. C. Pan, C. C. Chou, Jpn. J. Appl. Phys. **41**, 6679 (2002).
6. W. C. Lai, M. Yokoyama, S. J. Chang, J. D. Guo, C. H. Sheu, T. Y. Chen, W. C. Tsai, J. S. Tsang, S. H. Chan, S. M. Sze, Jpn. J. Appl. Phys. **39**, L1138 (2000).
7. A. Grabowski, J. Jaglarz, M. Nowak, Opt. Laser Technol. **30**, 183 (1998).
8. G. K. Bhaumik, A. K. Nath, S. Basu, Mater. Sci. Eng. B-Solid State Mater. Adv. Technol. **52**, 25 (1998).
9. V. S. Serbesov, P. A. Atanasov, R.I. Tomov, J. Mater. Sci.-Mater. Electro. **5**, 272 (1994).
10. C. J. Lin, G.-R. Lin, Y. L. Chueh, L. J. Chou, Electrochem. Solid-State Lett. **8**, D43 (2005).
11. L. Khriachtchev, M. Räsänen, S. Novikov, Appl. Phys. Lett. **83**, 3018 (2003).
12. R. G. Elliman, M. J. Lederer, B. Luther-Davies, Appl. Phys. Lett. **80**, 1325 (2002).
13. X. Y. Chen, Y. F. Lu, L. J. Tang, Y. H. Wu, B. J. Cho, X. J. Xu, J. R. Dong, W. D. Song, J. Appl. Phys. **97**, 014913 (2005).
14. J. Hawkes, I. Latimer, Lasers: Theory and Practice, Prentice-Hall International Series in Optoelectronics, Hertfordshire, 1995.
15. D. A. G. Bruggeman, Ann. Phys. **24**, 636 (1935).
16. B. Abeles, J. I. Gittleman, Appl. Opt. **15**, 10 (1976).
17. A. En Naciri, M. Mansour, L. Johann, J. J. Grob, C. Eckert, Nucl. Instr. and Meth. B **216**, 167 (2004).
18. G. Vijaya Prakash, M. Cazzanelli, Z. Gaburro, L. Pavesi, F. Iacona, G. Franzò, F. Priolo, J. Mod. Opt. **49**, 719 (2002).
19. L. Khriachtchev, M. Rasanen, S. Novikov, L. Pavesi, Appl. Phys. Lett. **85**, 1511 (2004).

Downloaded From: http://proceedings.spiedigitallibrary.org/ on 04/26/2014 Terms of Use: http://spiedl.org/terms

20. F. Rochet, G. Dufour, H. Roulet, B. Pelloie, J. Perriere, E. Fogarassy, A. Slaoui, M. Froment, Phys. Rev. B **37**, 6468 (1999).
21. M. C. Rossi, S. Salvatori, F. Galluzzi, G. Conte, Mater. Sci. Eng. B **69-70**. 299 (2000).
22. E. D. Palik, Handbook of Optical Constants of Solids, Academic Press, Washington, 1985.
23. A. Janotta, Y. Dikce, M. Schmidt, C. Eisele, M. Stutzmann, M. Luysberg, L. Houben, J. Appl. Phys. 95, **4060** (2004).
24. B. Gallas, C.-C. Kao, S. Fisson, G. Vuye, J. Rivory, Y. Bernard, C. Belouet, Appl. Surf. Sci. **185**, 317 (2002).
25. G.-R. Lin and C. J. Lin, J. Appl. Phys. **95**, 8484 (2004).
26. G.-R. Lin, C. J. Lin, K. C. Yu, J. Appl. Phys. **96**, 3025 (2004).
27. H. S. Bae, T. G. Kim, C.N. Whang, S. Im, J.S. Yun, J.H. Song, J. Appl. Phys. **91**, 4078 (2002).
28. C. J. Lin, G.-R. Lin, IEEE J. Quantum Electron. **41**, 441 (2005).
29. J. C. Cheang-Wong, A. Oliver, J. Roiz, J. M. Hernánaez, L. Rodríguez-Fernández, J. G. Morales, A. Crespo-Sosa, Nucl. Instrum. Methods Phys. Res. B **175**, 490 (2001).
30. T. D. Bennett, D. J. Krajnovich, L. Li, J. Appl. Phys. **85**, 153 (1999).
31. G. Franzo, A. Irrera, E. C. Moreira, M. Miritello, F. Iacona, D. Sanfilippo, G. D. Stefano, P. G. Fallica, and F. Priolo, Appl. Phys. A **74**, 1 (2002).
32. A. Irrera, D. Pacifici, M. Miritello, G. Franzo, F. Priolo, F. Iacona, D. Sanfilippo, G. Di Stefano, and P. G. Fallica, Appl. Phys. Lett. **81**, 1866 (2002).
33. J. De La Torre, A. Souifi, A. Poncet, C. Busseret, M. Lemiti, G. Bremond, G. Guillot, O. Gonzalez, B. Garrido, J. R. Morante, and C. Bonafos, Physica E **16**, 326 (2003).
34. J. Valenta, N. Lalic, and J. Linnros, Opt. Mater. **17**, 45 (2001).
35. D. J. DiMaria, J. R. Kirtley, E. J. Pakulis, D. W. Dong, T. S. Kuan, F. L. Pesavento, T. N. Theis, J. A. Cutro, and S. D. Brorson, J. Appl. Phys. **56**, 401 (1984)
36. D. K. Ferry, S. M. Goodnick, in *Transport in Nanostructures*, (Cambridge University Press, New York, 1997), pp. 23-90.

Downloaded From: http://proceedings.spiedigitallibrary.org/ on 04/26/2014 Terms of Use: http://spiedl.org/terms